https://doi.org/10.5194/essd-2020-255
Preprint. Discussion started: 17 October 2020


Open Access Earth System Science Data Discussions

# Wind, waves, and surface currents in the Southern Ocean: Observations from the Antarctic Circumnavigation Expedition

Marzieh H. Derkani[1], Alberto Alberello[2,3], Filippo Nelli[1], Luke G. Bennetts[3], Katrin G. Hessner[4], Keith MacHutchon[5], Konny Reichert[6], Lotfi Aouf[7], Salman Saeed Khan[8], and Alessandro Toffoli[1]

[1]Department of Infrastructure Engineering, The University of Melbourne, 3010, Melbourne, VIC, Australia
[2]Department of Physics, University of Turin, 10125, Turin, Italy
[3]School of Mathematical Sciences, University of Adelaide, 5005, Adelaide, SA, Australia
[4]OceanWaveS GmbH, 21339 Lüneburg, Germany
[5]Depertment of Civil Engineering, University of Cape Town, 7701, Cape Town, South Africa
[6]Independent Scholar, 6021 Wellington, New Zealand
[7]Météo-France, 31100, Toulouse, France
[8]Oceans and Atmosphere, Commonwealth Scientific and Industrial Research Organisation, 3195, Aspendale, VIC, Australia

**Correspondence:** Marzieh H. Derkani (marzieh.h.derkani@gmail.com) and Alessandro Toffoli (toffoli.alessandro@gmail.com)

**Abstract.**

The Southern Ocean has a profound impact on the Earth's climate system. Its strong winds, intense currents, and fierce waves are critical components of the air-sea interface and contribute to absorbing, storing, and releasing heat, moisture, gasses, and momentum. Owing to its remoteness and harsh environment, this region is significantly under sampled, hampering the validation of prediction models and large scale observations from satellite sensors. Here, an unprecedented data set of simultaneous observations of winds, surface currents, and ocean waves is presented, to address the scarcity of in situ observations in the region—http://dx.doi.org/10.26179/5ed0a30aaf764 (Alberello et al., 2020c), and http://dx.doi.org/10.26179/5e9d038c396f2 (Derkani et al., 2020). Records were acquired underway during the Antarctic Circumnavigation Expedition (ACE), which went around the Southern Ocean from December 2016 to March 2017 (Austral summer). Observations were obtained with the wave and surface current monitoring system WaMoS-II, which scanned the ocean surface around the vessel using marine radars. Measurements were assessed for quality control and compared against available satellite observations. The data set is the most extensive and comprehensive collection of observations of surface process for the Southern Ocean and has the potential to support further theoretical and numerical research on lower atmosphere, air-sea interface and upper ocean processes.

## 1 Introduction

The Southern Ocean comprises an uninterrupted band of water around Antarctica south of the 60$^{th}$ parallel. More broadly, it refers to the body of water south of the main landmasses of Africa, Australia, and South America, with a northern limit

https://doi.org/10.5194/essd-2020-255
Preprint. Discussion started: 17 October 2020


Open Access Earth System Science Data Discussions

at approximately 40° South (see, for example, Young et al., 2020). This region is dominated by strong westerly winds, the notorious roaring forties, furious fifties and screaming sixties (Lundy, 2010). They fuel the Antarctic Circumpolar Current (the world's largest ocean current, e.g. Park et al., 2019), which mixes warm waters descending from the Atlantic, Indian and Pacific Oceans with northward cold streams from the Antarctic. Above all, intense winds give raise to some of the fiercest waves on the planet (e.g Barbariol et al., 2019; Vichi et al., 2019; Young and Ribal, 2019; Young et al., 2020). Acting as an interface between the lower atmosphere and the upper ocean, waves entrap and release momentum, heat, moisture and gasses through breaking (Melville, 1996; Csanady, 2001; Veron, 2015) and drive air-sea fluxes (e.g. Humphries et al., 2016; Schmale et al., 2019; Thurnherr et al., 2020). Due to almost unlimited fetches (the distance of open water over which the wind blows), Southern Ocean waves are normally long and fast moving, allowing them to inject turbulent motion throughout the water column down to depths of 100–150 m, i.e. approximately half wavelength, and contributing to ocean mixing (Babanin, 2006; Qiao et al., 2016; Toffoli et al., 2012; Alberello et al., 2019b). The combined effect of the Antarctic Circumpolar Current, which cools and sinks near-surface water, and waves, which regulate fluxes and stir the upper ocean, produces a well mixed layer that extends from about 100 m in the summer months to about 500 m in the winter months (e.g. Dong et al., 2008). This deep mixed layer gives the Southern Ocean capacity to store more heat and gasses than any other latitude band on the planet, making this remote ocean a major driver of the Earth's climate system (see, for example, Dong et al., 2007).

South of the 60$^{th}$ parallel, a strong sea ice seasonal cycle of advance and retreat (Eayrs et al., 2019) forms an integral part of a coupled atmosphere–sea–ice–ocean system and influences Southern Ocean dynamics. Sea ice extent around Antarctica impacts albedo, atmospheric and thermohaline circulation, and ocean productivity (Perovich et al., 2008; Massom and Stammerjohn, 2010; Notz, 2012), contributing to the heat balance. Further, it attenuates waves, modulating air-sea fluxes and mixing (Thomas et al., 2019). In turn, waves (in combination with wind) have a significant feedback to the Antarctic sea ice state, extent, and thickness (e.g Wadhams, 1986; Bennetts et al., 2017; Alberello et al., 2019a; Vichi et al., 2019; Alberello et al., 2020a).

In situ observations of atmospheric and oceanographic properties are scarce due to the remoteness of the region. Although there have been many expeditions crossing the Southern Ocean (see a general overview in Schmale et al., 2019), measurements have primarily been taken en-route to Antarctic stations, leaving entire sectors undersampled. Further, measurements normally concentrate on the lower atmosphere and/or the upper ocean (not necessarily concomitantly), while waves are generally not monitored. Only a handful of buoys have operated in the region: (i) the Southern Ocean Flux Station (Schulz et al., 2011, 2012), a meteorological buoy first deployed in 2010 at approximately 350 nautical miles south-west of Tasmania (Australia) that provides observations of meteorological parameters, including the directional wave spectrum, downwelling radiation, and sea water temperature and salinity; (ii) the Southern Ocean wave buoy network, which comprises of one directional wave buoy deployed south of Campbell Island (New Zealand) and five drifting buoys (Barbariol et al., 2019); and (iii) the Global Southern Ocean Array and the Global Argentine Basin Array, which are networks of fixed and moored platforms and mobile profilers (gliders) deployed South-West of Chile and in the Argentinian basin, respectively, to monitor waves, air-sea fluxes of heat, moisture and momentum, and physical, biological and chemical properties throughout the water column (Trowbridge et al., 2019). Buoys have also been deployed in the Antarctic marginal ice zone to monitor waves-in-ice and sea ice drift (e.g. Meiners et al., 2016; Ackley et al., 2020; Meylan et al., 2014; Vichi et al., 2019; Alberello et al., 2020a).

https://doi.org/10.5194/essd-2020-255
Preprint. Discussion started: 17 October 2020


Open Access Earth System Science Data Discussions

A database covering the Southern Ocean more uniformly is provided by polar orbiting microwave radar satellites such as Altimeters, Scatterometers, and Synthetic Aperture Radar (SAR). Nevertheless, sea state observations are scattered in both space and time due to the nature of polar satellite orbits, and normally limited to average wind and current speeds, and wave heights. SAR technology provides images that can be converted into directional wave energy spectra. However, SAR only detects swell systems, i.e. long-wave systems no longer under the effect of local winds, and with wavelengths longer than 115 m (Collard et al., 2009). It does not resolve the most relevant wind sea, i.e. the short-wave components directly generated by local winds. This limitation is partly addressed by the recently launched Chinese French Oceanography Satellite (CFOSAT) mission, which detects wave systems with wavelengths longer than 70 m (Hauser et al., 2020).

The scarcity of in situ observations has a negative feedback on the satellite network, which cannot rely on sufficient ground truth to be validated with high confidence. In turn, this drawback impacts prediction models, which are impaired by notable biases in the Southern Ocean (see, for example, Yuan, 2004; Li et al., 2013; Zieger et al., 2015). To address the lack of in situ observations and support calibration and validation of satellite sensors and prediction models, an international initiative, organised by the Swiss Polar Institute, led an unprecedented circumnavigation of the Antarctic continent (the Antarctic Circumnavigation Expedition, ACE; Walton and Thomas, 2018) during the Austral summer of 2016–2017. The objective of the expedition was to sample concomitant processes in the lower atmosphere, at the ocean surface and in the upper ocean layers all around the Antarctic continent in a single season (Rodríguez-Ros et al., 2020; Schmale et al., 2019; Smart et al., 2020; Thurnherr et al., 2020). Here we present the database of underway sea state observations, comprising of concurrent records of winds, surface currents and waves. In Sections 2 and 3, details of the expedition, the instrumentation, and its calibration are presented. An overview of the database is presented in Section 4. A comparison against available satellite data and an assessment of uncertainties is given in Section 5. Concluding remarks are made in the last section.

## 2 The Antarctic Circumnavigation Expedition

ACE took place from 20 December 2016 to 19 March 2017, encompassing the entire Austral summer. It consisted of a voyage around the Southern Ocean between 34° and 74° South aboard the Russian research icebreaker Akademik Tryoshnikov (see technical details in Walton and Thomas, 2018).

The voyage was divided into three legs. The first one (leg 1) was along the Indian Ocean from Cape Town, South Africa, to Hobart, Australia, with stops at Marion Island, Iles de Crozet et Kerguelen and Heard Island. Leg 2 went across the Pacific Ocean to Punta Arenas, Chile, with stations at Mertz glacier, Balleny Islands, Scott Island, Mount Siple (the southernmost station), Peter I Island and Diego Ramirez. The final one (leg 3) crossed the Atlantic Ocean back to Cape Town via South Georgia, South Sandwich Islands and Bouvetøya. In addition, scientific observations were carried out during transit across the Atlantic on the way to/from South Africa (leg 0 and 4, respectively).

A schematic of the expedition is presented in Fig. 1 and photos of the environmental conditions in Fig. 2. Legs 1 and 3 mostly covered the open ocean north of the 60$^{th}$ parallel, roughly between the sub-Antarctic and Polar fronts delimiting the Antarctic Circumpolar Current (Figs. 2a and b). Leg 2 primarily concentrated on the Antarctic marginal ice zone (see Fig. 2c)

https://doi.org/10.5194/essd-2020-255
Preprint. Discussion started: 17 October 2020


Open Access Earth System Science Data Discussions

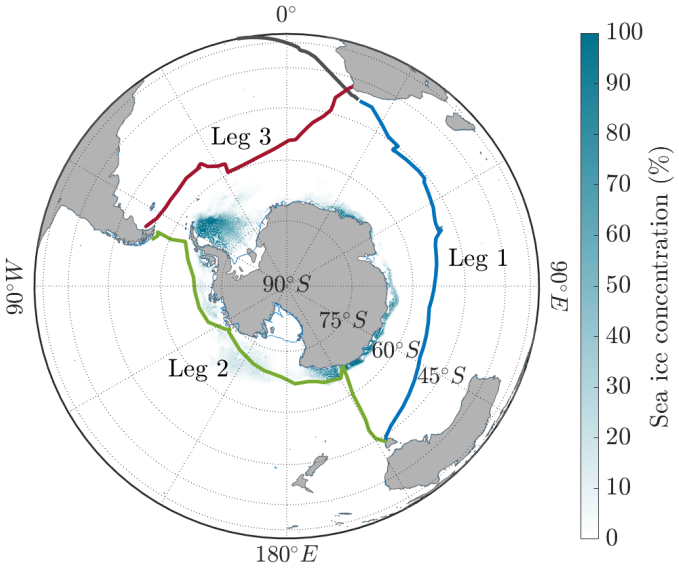


**Figure 1.** Map of the ACE voyage divided by legs. Average sea ice concentration during the expedition is also shown.

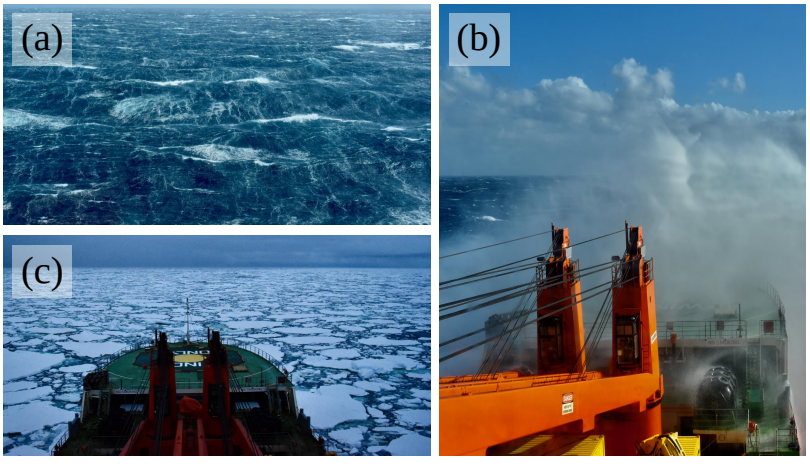


**Figure 2.** Examples of sea states conditions: ocean surface during storm conditions (a); sailing through a storm (b); the marginal ice zone (c).

south of the 60$^{th}$ parallel, with two transects across the Western Pacific Ocean sector south of Tasmania and the Drake Passage at the beginning and at the end of the leg. Average sea ice extent during ACE as detected by the Advanced Microwave Scanning Radiometer 2 sensor is shown in Fig. 1.

https://doi.org/10.5194/essd-2020-255
Preprint. Discussion started: 17 October 2020


Open Access Earth System Science Data Discussions

## 3 The sea state monitoring system

### 3.1 Instrumentation and technical configuration

Sea state observations were recorded with the wave and surface current monitoring system WaMoS-II (details on software, hardware and measurement principles can be found in Reichert et al., 1999). The instrument uses the marine X-band radar (9.41 GHz)—a standard equipment on any vessels—to acquire high-definition radar images of the surrounding ocean surface and derive the directional wave energy spectrum, related integral parameters such as the significant wave height and mean wave period and surface current speed and direction. The overall system consists of an A/D converter, a PC, and a processing software connected to the X-band radar (a schematic of WaMoS-II is presented in Fig. 3a). In addition, true wind velocity and direction from the ship's meteorological station, water depth from the echo-sounder and ship's positions, speed, and course from a Global Positioning System (GPS) receiver are fed into the system.

The basic configuration for the X-band radar requires an antenna with rotation speed of 24 rpm, horizontal opening angle of 0.9°, and radar pulse width of 80 ns. In addition, the radar has to be operated in the near range, i.e. 1.5 nautical miles (≈ 2.8 km). This allows WaMoS-II to acquire a radar image with a spatial resolution of 12 m and an angular resolution of 0.9° for every radar rotation (a sample image is reported in Figure 3b).

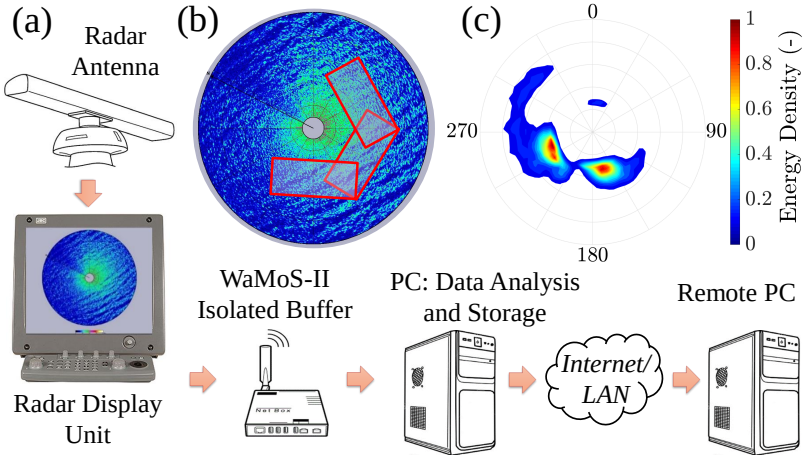


**Figure 3.** Schematic of the wave and surface current monitoring system WaMoS-II (a); example of radar imagery and sub-areas (not in scale) for post-processing (b); and a sample derived directional wave energy spectrum (c).

### 3.2 Measurement principles

The marine radar forms images of the surrounding area based on the backscatter of radar beams. The short wavelets (ripples) on the ocean surface contribute notably to reflection, while long wave components modulate the returning signal. This results in stripe-like patterns in the radar images that correspond to the waves. The system can only operate with wind speeds greater

https://doi.org/10.5194/essd-2020-255
Preprint. Discussion started: 17 October 2020


Open Access Earth System Science Data Discussions

than 3 m/s, which ensure the ocean surface is rough enough (i.e. ripples are developed) to backscatter the signal efficiently (Hatten et al., 1998).

The basic input for extracting sea state features is a sequence of 64 consecutive images. Post processing is carried out on sub-areas of 600 m×1200 m normally taken in front of the vessel, at port and at starboard to avoid contamination due to the ship's wake (an example of sub-areas is presented in Fig. 3b). The temporal sequence for each sub-area, $I(x,y,t)$, is transformed with a Discrete Fourier Transform into its spectral domain counterpart, i.e. a three-dimensional image spectrum $I^{(3)}(k_x,k_y,\omega)$, where $\overrightarrow{k}=(k_x,k_y)$ is the two dimensional wavenumber vector and $\omega$ is the angular frequency. Assuming linear wave theory (Holthuijsen, 2007), spectral components in $I^{(3)}(k_x,k_y,\omega)$ that correspond to ocean waves have to satisfy the linear dispersion relation

$$\omega=\sqrt{g|\overrightarrow{k}|\tanh(|\overrightarrow{k}|d)}+\overrightarrow{k}\overrightarrow{u}, \tag{1}$$

where $g$ is the acceleration due to gravity, $d$ is the water depth, $\overrightarrow{u}$ is the surface current and $|\overrightarrow{k}|=\sqrt{k_x^2+k_y^2}$ is the two dimensional wavenumber. Spectral components that do not obey equation (1) are assumed to be noise and hence removed. The remaining three-dimensional image spectrum is integrated over the positive frequency domain and corrected to remove shadowing and tilting effects, resulting in the directional wave energy spectrum $E_r(k_x,k_y)$. The latter is expressed as a function of wave frequency $f=\omega/2\pi$ and direction $\vartheta$ in WaMoS-II's standard output; the change of variable from wavenumbers to frequency-directions satisfies the dispersion relation in equation (1). An ensemble average over the sub-areas is computed.

The primary wave spectrum $E_r(f,\vartheta)$ is not scaled correctly, because it depends on the radar backscatter rather than water surface elevation. Therefore, its zero-th order moment represents the signal-to-noise-ratio ($SNR$), instead of the variance of the surface elevation ($m_0$). To re-scale the wave spectrum, $SNR$ is converted into $m_0$ with a linear regression equation (see Young et al., 1985, for details):

$$m_0=A+B\sqrt{SNR}, \tag{2}$$

where $A$ and $B$ are empirical constants that have to be calibrated following installation. Energy at each spectra modes is corrected accordingly to derive the final wave energy spectrum $E(f,\vartheta)$ (see an example in Fig. 3c).

Wave parameters are derived by integrating $E(f,\vartheta)$. These include the significant wave height, dominant and mean wave periods, associated wavelengths, directional width and mean wave direction (see Appendix A for a full list of parameters and their definitions). WaMoS-II also partitions the directional wave energy spectrum to derive wave heights and periods for wind sea and the first three swell systems.

Ocean currents induce a Doppler shift to the wave field. Both current speed and direction can be quantified by minimising the distance between the position of the spectral energy in $I^{(3)}(k_x,k_y,\omega)$ and the theoretical position given by equation (1) using least squares techniques (Young et al., 1985). The vessel's forward speed and heading are used to derive the true current.

Rain, snow and sea ice produce an excess signal backscatter, which affects the quality of the resulting radar image and thus accuracy. WaMoS-II automatically assesses the reliability of images with an Internal Quality index (IQi) (Hessner et al., 2019). Low quality images are automatically excluded from post processing.

https://doi.org/10.5194/essd-2020-255
Preprint. Discussion started: 17 October 2020


Open Access Earth System Science Data Discussions

### 3.3 Underway observations and file types

WaMoS-II operated continuously to record observations of the sea state during ACE. The vessel was equipped with one X-band radar, which was shared between science (requiring short range settings) and navigational aid (operating at medium and long range). Therefore, data acquisition was interrupted anytime the radar was needed for navigation, resulting in gaps in the observations. This was most common during leg 2, as the radar was often switched to long range to detect icebergs.

The wave spectrum $E(f,\vartheta)$ was sampled at 160 s, assuming no gaps or corrupted images occur during the sampling of 64 consecutive radar images. Output files consist of: (i) the directional wave-energy spectrum in the wavenumber domain ($E(k_x,k_y)$, file extension D2S) and frequency–directional domain ($E(f,\vartheta)$, file extension FTH); and (ii) the (single) one-dimensional frequency–energy spectrum $S(f)$ obtained by integrating the directional spectrum $E(f,\vartheta)$ over $\vartheta$ (file extension D1S). Each file also includes a header that provides metadata such as geographical references (latitude and longitudes), time, wind speed and direction, ship speed and heading, current speed and direction, plus additional integrated parameters.

WaMos-II also performed a running average over 20 minutes to minimize the effects of natural variability. Output files consist of: (i) the mean directional wave-energy spectrum in both wavenumber and frequency–directional domain (file extensions D2M and FTM, respectively); and (ii) the mean one-dimensional frequency–energy spectrum (file extension D1M). These files are sampled every 160 s, with the first one 20 minutes after starting the equipment.

In addition, time series of wind, current and wave variables from mean directional wave spectra are archived in monthly summary files.

### 3.4 Calibration

The calibration of coefficients $A$ and $B$ in equation (2) was performed by forcing the signal-to-noise-ratio to match independent (benchmark) observations of $m_0$. The benchmark values were reconstructed from records of ship motion, which were measured throughout the expedition with an Inertial Measurement Unit (IMU) at a sampling rate of 1 Hz (Alberello et al., 2020b).

An overview of ship motion to sea state conversion can be found in e.g. Milne and Zed (2018). The method relies on the principle that the vessel is a rigid body with six degrees of freedom (three translations: heave, surge and sway; and three rotations: pitch, roll and yaw) that moves in response to the incident wave field expressed as the frequency spectrum $S(f) = \int E(f,\vartheta)\,\mathrm{d}\vartheta$, and restoring forces as a function of its mass, geometry, loading conditions, and forward speed, among other parameters. The relation between the ship motion and the wave field is evaluated via the response amplitude operator $R(f)$, i.e. a ship-specific function that translates the motion spectrum $S_{ship}(f)$ into the wave spectrum: $S(f) = S_{ship}(f)/R(f)^2$. Motion spectra were evaluated by applying a Fourier Transform to 160 s time series. An approximation of $R(f)$ for the Akademik Tryoshnikov was calculated solving the equation of motion with a model based on a boundary element method (NEMOH, Babarit and Delhommeau, 1968). The variance of the surface elevation is then calculated from the derived $S(f)$ as $m_0 = \int S(f)\mathrm{d}f$.

Coefficients $A$ and $B$ in equation (2) were estimated using a maximum likelihood method for the period 9–11 December 2016 (leg 0). The root mean square error ($RMSE$) of the fit is 0.21 m with correlation coefficient $R \approx 0.90$, and scatter index

https://doi.org/10.5194/essd-2020-255
Preprint. Discussion started: 17 October 2020


Open Access Earth System Science Data Discussions

$SI \approx 0.1$. Time series of $m_0$ derived from the IMU sensor and calibrated $m_0$ from WaMoS-II are shown in Fig. 4. Calibrated $A$ and $B$ coefficients were subsequently used to re-scale individual modes of the energy spectrum.

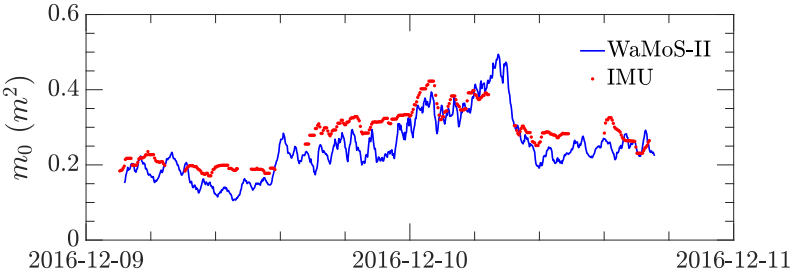


**Figure 4.** Time series of spectral variance $m_0$: benchmark observations derived from ship motion data (red dots) and calibrated records from WaMoS-II (blue solid line).

## 4 Overview of sea state conditions

### 4.1 Sea state climate during ACE

Excluding the regions south of the 60$^{th}$ parallel, which undergoes a strong seasonal sea ice cycle (Eayrs et al., 2019), the Southern Ocean is normally characterised by weak seasonal variability (Young et al., 2020). Therefore, extreme sea states remain likely even during summer. As a reference, wind, current and wave climate statistics in the form of the 50$^{th}$ and 90$^{th}$ percentiles (hereafter P50 and P90, respectively) aggregated in $2^\circ \times 2^\circ$ regions for the summer months (December, January, February) are reported in Fig. 5. Data are from all satellite missions mounting altimeter sensors that are available from 1985 to 2019 for wind speed and wave height (Ribal and Young, 2019) and from 1993 to 2019 for surface current speed (Rio et al., 2014).

The wind speed is represented by its value at 10-metre above sea level ($U_{10}$). Apart from a region East of Argentina, where the South American continent induces a shadowing effect, wind speed is fairly uniform throughout the ocean: P50 varies between 10 and 12 m/s, while P90 ranges between 15 and 18 m/s (see Figs. 5a and b). Close to the Antarctic continent and outside the belt of the strong westerly winds (south of the 70$^{th}$ parallel), wind speed weakens with P50 reducing to $\approx$ 3 m/s and P90 to $\approx$ 10 m/s. There are also low wind speeds ($U_{10} < 3$ m/s for both P50 and P90) in the lee of the Antarctic peninsula, although this may relate to uncertainties related to a high concentration of sea ice (see Fig. 1) and/or the increased drag over sea ice compared to open water (Martinson and Wamser, 1990). Note that, excluding the station at Mount Siple, the expedition remained within the belt of westerly winds.

Significant wave height $H_s$ follows the wind pattern, underpinning the dominance of wind seas on swell systems. Between 40° and 60° South, the belt where most of legs 1 and 3 took place, the P50 $\approx$ 3.5 m and P90 ranges between 5 and 6 m (Figs. 5c and d). There is an evident shadowing effect east of the Drake passage, due to a combination of lower wind speed and a reduction of fetches. South of the 60$^{th}$ parallel (Leg 2), $H_s$ drops notably with the P50 decreasing to $\approx$ 2 m and P90 reducing

https://doi.org/10.5194/essd-2020-255
Preprint. Discussion started: 17 October 2020


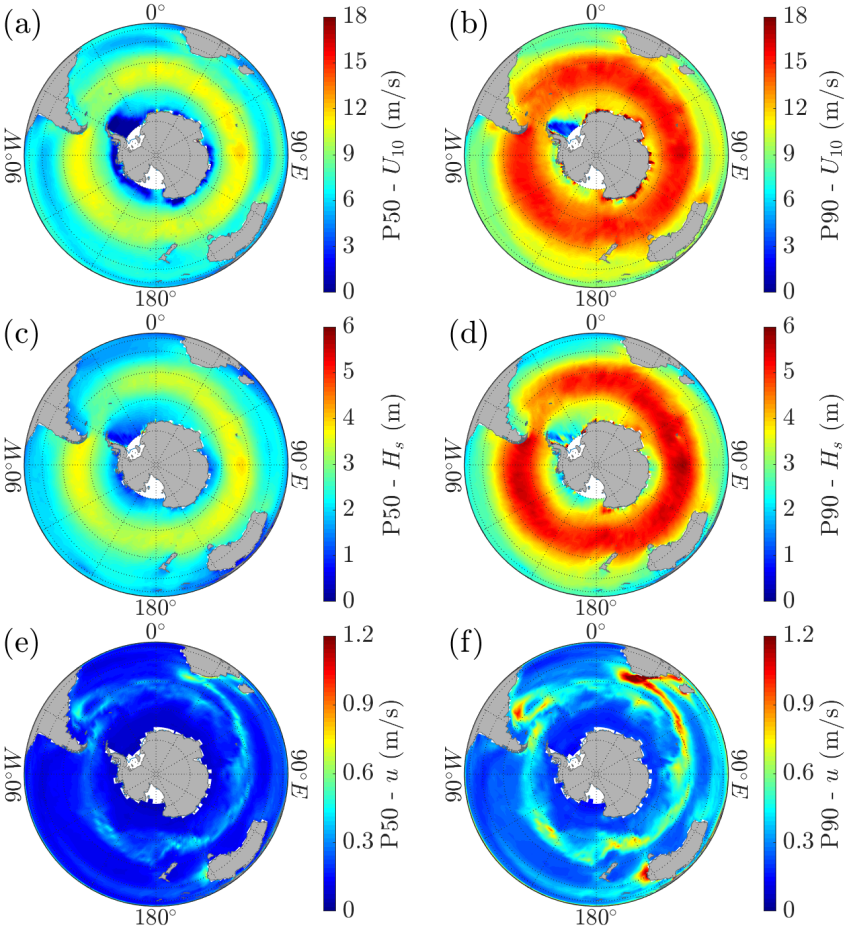


**Figure 5.** Wind speed ($U_{10}$), significant wave height ($H_s$), and surface current speed ($u$) climatology in austral summer: (a) 50$^{th}$ percentile (median) wind speed, (b) 90$^{th}$ percentile wind speed, (c) 50$^{th}$ percentile (median) significant wave height, (d) 90$^{th}$ percentile significant wave height, (e) 50$^{th}$ percentile (median) surface current speed, (f) 90$^{th}$ percentile surface current speed.

195 to ≈ 4 m, despite strong westerly winds being active down to 70° South. The attenuation is induced by sea ice (Bennetts et al., 2015; Toffoli et al., 2015; Montiel et al., 2016), which has high concentration close to the Antarctic coastline, even in the summer months, especially in the West Pacific, Ross sea and Amundsen sea sectors of Antarctica (see Fig. 1).

The speed of the Antarctic Circumpolar Current has P50 ≈ 0.5 m/s. The P90 shows velocity with maxima in excess of 0.75 m/s, especially in the Indian Ocean sector (first half of leg 1). Besides the Antarctic Circumpolar Current, ACE crossed
200 two regions with strong currents: the Agulhas region, where P90 excess 1.5 m/s; and the Argentine basin (beginning of leg 3), where a northward extension of the Antarctic Circumpolar Current forces water flow to speeds of approximately 1 m/s. South of the polar front (leg 2), there are no significant circulation patter, with maximum current speed less than 0.3 m/s.

https://doi.org/10.5194/essd-2020-255
Preprint. Discussion started: 17 October 2020


Open Access Earth System Science Data Discussions

### 4.2 Observed sea states during ACE

Figure 6 shows time series of the observed sea state conditions—10 m true wind speed ($U_{10}$), significant wave height ($H_S$), mean wave period ($T_{m-10}$), wave directional spreading ($\sigma_\theta$), inverse wave age ($\mu$), wave steepness ($\varepsilon$) and current speed ($u$)—throughout the expedition. Definitions of the variables are reported in Appendix A. As a benchmark, collocated values of P50 and P90 for wind speeds, significant wave heights and current speeds, are also reported in figure 6.

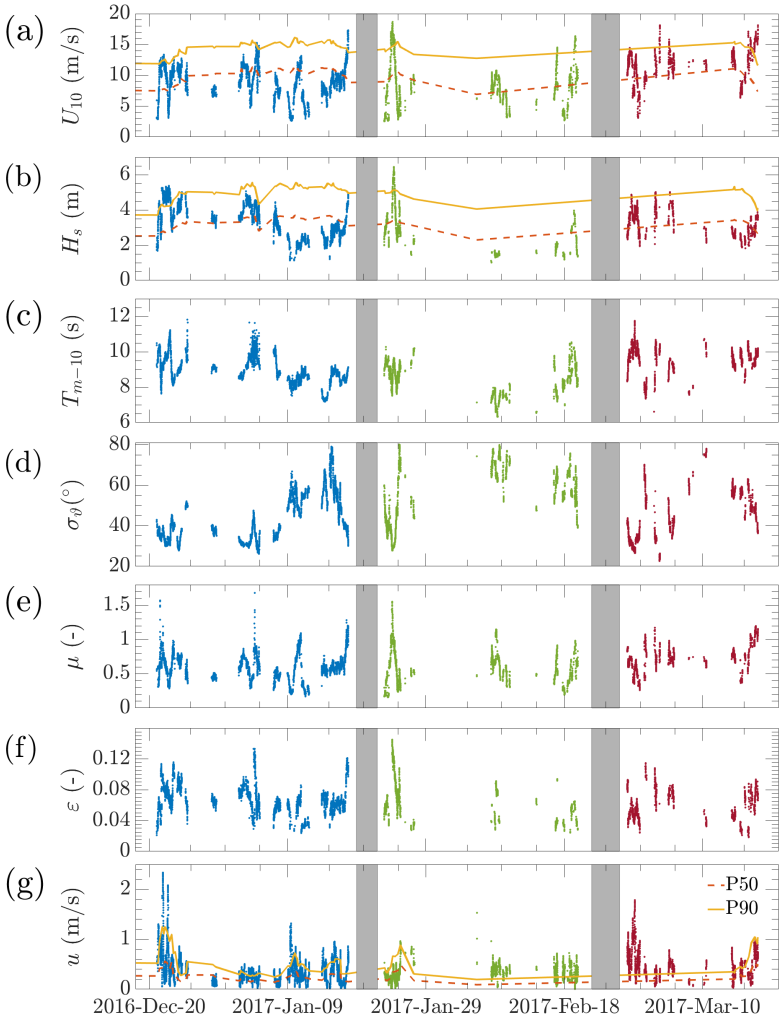


**Figure 6.** Time series of sea state variables in leg 1 (blue), leg 2 (green), and leg 3 (red): wind speed (a); significant wave height (b); mean wave period (c); mean directional spread (d); inverse wave age (e); wave steepness (f); and current speed (g). Details of variables are reported in Appendix A. Climate statistics derived from satellite observation for wind speed, significant wave height and current speed are shown: 50$^{th}$ (dashed line) and 90$^{th}$ (solid line) percentile.

https://doi.org/10.5194/essd-2020-255
Preprint. Discussion started: 17 October 2020


Open Access Earth System Science Data Discussions

Overall, the observed median wind speed was 7.25 m/s with an interquartile ($IQ$) of 5.1 m/s. During leg 1, the expedition went through six storm events with wind speeds reported in excess of 12 m/s (P50 $\approx$ 10 m/s). Two of these events were equal to or greater than the P90 for the season ($\approx$ 15 m/s). Leg 2 started with the most extreme storm during ACE; wind reached speeds close to 20 m/s, which is well above P90. The remainder of leg 2 was characterised by relatively low wind speeds, consistent with P50. Two more storms with wind speeds in excess of P90 were encountered at the end of leg 2, while approaching and crossing the Drake Passage. The final leg was also characterised by intense storms with wind speeds notably above P50 for almost the entire leg. Three significant storm events with wind speeds above P90 ($U_{10} \approx 18$ m/s) were reported.

The median significant wave height during the expedition was 2.61 m and $IQ \approx 1.6$ m. To avoid the most energetic waves, the ship's course was continuously adapted to bypass storms. Despite this, intense wave conditions were encountered with $H_s$ reaching the P90 ($\approx$ 5 m) during almost all storm events, especially during leg 1 and leg 3. The largest waves ($H_s > 6$ m) were encountered at the beginning of leg 2 (see photos of the sea state in Figs. 2a and b). Thereafter, $H_s$ was less than 2 m as a result of the interaction with sea ice (see Figs. 2c). The crossing of the Drake passage at the end of leg 2 did not record significantly large waves, with $H_s \approx 4$ m at most. Wave periods were generally long and normally in excess of 8 s ($\approx$ 100 m wavelengths), substantiating the extensive (almost infinite) fetches for wave development. Concomitantly with almost all storms, $T_{m-10}$ increased and reached maximum values of 11–12 s (wavelengths $\approx$ 200 m).

An intrinsic feature of oceanic sea states is the directional distribution of the spectral density function (Toffoli et al., 2017; Fadaeiazar et al., 2020), which is summarised in the form of a mean directional spreading (i.e. the circular standard deviation of the directional wave energy spectrum). Sea states dominated by strong winds are normally characterised by a broad spreading with $\sigma_\vartheta > 40°$ (Donelan et al., 1985). These conditions were reported consistently throughout the expedition, with maximum mean directional spreading reaching values as large as 80°. Narrow directional distributions ($\sigma_\vartheta \leq 30°$) were also common though and primarily recorded in between storms, where the sea state was dominated by swells.

The inverse wave age $\mu$ and the wave steepness $\varepsilon$ are parameters that estimate the stage of growth of the wave field. To some extent, both variables are associated to nonlinear mechanisms that lead to large (extreme) waves (Onorato et al., 2009; Toffoli et al., 2017), and wave breaking (Toffoli et al., 2010), and, thus, ocean–atmosphere fluxes (Schmale et al., 2019; Thurnherr et al., 2020). The inverse wave age is the ratio of wind speed to wave phase velocity (i.e. the ratio of wavelength to period). Following their generation, waves grow in height and length until they move faster than winds (Holthuijsen, 2007). For $\mu > 0.8$, waves are "young" as they are in a growing phase. This conditions is normally characterised by a steep profile, which leads to breaking. Young waves were recorded during all storm events with steepness generally in excess of 0.1. For $\mu < 0.8$, the waves no longer receive energy from wind as they have reached full development. The shape of waves is gently sloping (i.e. the wave steepness is small) and breaking is unlikely (the ocean is dominated by swell). During the most extreme events at the beginning of leg 2, steepness reached a maximum of about 0.13. This is an exceptionally high value for ocean waves and is normally associated to the formation of rogue waves (Onorato et al., 2009; Toffoli et al., 2010).

The majority of legs 1 and 3 followed the Antarctic Circumpolar Current with records of surface current speeds oscillating around 0.5 m/s. Interestingly, observations were notably higher than P90 for the majority of the expedition. Despite being primarily south of the polar front, currents faster than P90 were also recorded in leg 2, primarily in the marginal ice zone. ACE

https://doi.org/10.5194/essd-2020-255
Preprint. Discussion started: 17 October 2020




crossed two regions characterised by strong surface currents: East of South Africa at the southernmost edge of the Agulhas current (beginning of leg 1), with speeds up to 2 m/s; east of South America where the Antarctic Circumpolar Current has a northward extension, with surface speeds recorded up to 1.8 m/s.

## 5 Comparison against satellite observations

### 5.1 Wind speed and significant wave height

Wind speeds and significant wave heights are compared against collocated satellite observations from altimeter sensors (same data source discussed in the previous session). Due to the scattered nature of satellite data, average values are computed for clusters with spatial resolution of $\Delta X = \Delta Y = 0.5°$ and temporal resolution of $\Delta t = 3$ h. Although satellite observations have been quality controlled and calibrated against available in-situ sensors (see details in Ribal and Young, 2019), the scarcity of in-situ data in the Southern Ocean leaves uncertainties in the data set.

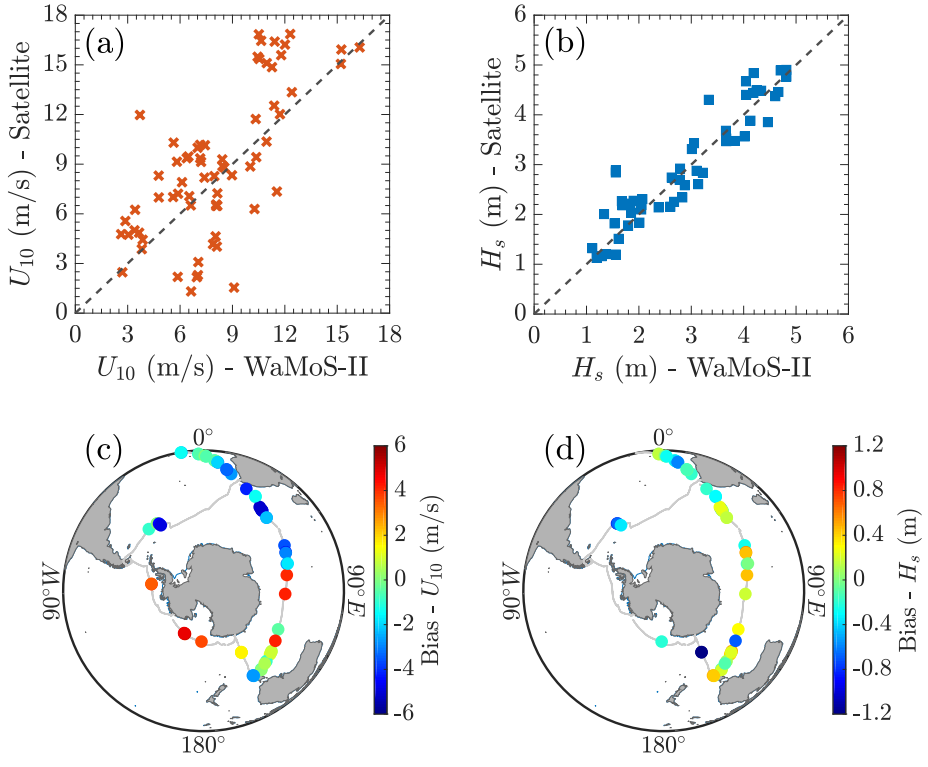


**Figure 7.** Wind and significant wave height from WaMoS-II versus satellite observations: scatter diagrams (panels a and b); and geographical distribution of biases (panels c and d).

https://doi.org/10.5194/essd-2020-255
Preprint. Discussion started: 17 October 2020


Fig. 7 shows scatter diagrams of matching averages at collocated clusters (panels a and b) and geographical distributions of biases (difference between WaMoS-II and satellite observations, panels c and d). Overall, in-situ measurements of wind speeds during ACE are consistent with concurrent satellite observations, with data laying along the 1:1 correlation line (wind observations are also in agreement with reanalysis data from the ERA-5 archive; Landwehr et al., 2020). Nevertheless, there is a notable $RMSE \approx 3.2$ m/s, with $R \approx 0.70$ and $SI \approx 0.360$. Biases show both over (especially at the beginning of leg 1 and leg 3) and under (at the end of leg 1 and leg 2) estimations of satellite observations, varying between -6 and 6 m/s. The most substantial positive biases are reported in the marginal ice zone, where Antarctic sea ice affects wind speed detection.

Significant wave heights match better with satellite observations than wind speeds: $RMSE \approx 0.42$ m, $R \approx 0.93$, and $SI \approx 0.155$. Most of collocated observations were found in leg 1. Overall, the bias is positive, indicating an slight under estimation of the sea state from satellite sensors. The largest biases (ranging between 0.4 and 1.2 m) were linked to storm events and are $\approx 10\%$ of the in-situ measured values.

### 5.2 Directional wave spectrum

Altimeter sensors only measure specific variables, namely the significant wave height and the wind speed, whereas SAR imagery can be converted into a directional wave energy spectrum (e.g Collard et al., 2009). Collocated SAR spectra from Sentinel-1A/1B missions within area of $0.5° \times 0.5°$ and maximum temporal difference of 6 h were retrieved from the Australian Ocean Data Network (AODN) portal (Khan et al., 2020). Overall, ten SAR spectra were found during ACE, with $\approx 70\%$ of them in the Indian Ocean during leg 1.

Example of corresponding wave spectra from WaMoS-II and SAR are presented in Fig. 8. The overall spectral shape agrees well, particularly the portion around the most energetic peak. Notable discrepancies, however, are evident for less energetic secondary peaks, for which the relative uncertainty grows.

To provide a more robust comparison, scatter diagrams for $H_s$, $T_{m-10}$ and $\sigma_\vartheta$ are presented in Fig. 9. For consistency, wave spectra from WaMoS-II have been filtered to eliminate high frequency modes that are not detected by SAR ($f > 0.117$ Hz or wavelength $L < 115$ m). SAR and WaMoS-II observations agree well, with $RMSE \approx 0.36$ m, $R \approx 0.92$, and $SI \approx 0.20$ for $H_s$; $RMSE \approx 0.42$ s, $R \approx 0.92$, and $SI \approx 0.038$ for $T_{m-10}$, noting wave periods from SAR are consistently (slightly) higher than WaMoS-II's; and $RMSE \approx 13.41°$, $R \approx 0.56$, and $SI \approx 0.295$ for $\sigma_\vartheta$, despite two outliers.

### 5.3 Surface current

Figure 10 shows the scatter diagram comparing surface current speeds from WaMoS-II and collocated observations derived from altimeter sensors (Rio et al., 2014). The geographical distributions of current speeds, directions and concurrent differences between WaMoS-II and altimeter sensors are presented in Figure 11. Note that values in both figures represent averages of observations falling in clusters of $0.5° \times 0.5°$ with temporal resolution of 0.5 h.

Contrary to wind and wave parameters, current speeds from WaMoS-II show notable differences from satellite observations. The former produces current speeds that are about 30% larger than the latter. Other basic metrics of the scatter diagram are: $RMSE \approx 0.2$ m/s; $R \approx 0.63$; and $SI \approx 0.80$. Bias associated to current speed are uniformly distributed across the expedition.

https://doi.org/10.5194/essd-2020-255
Preprint. Discussion started: 17 October 2020


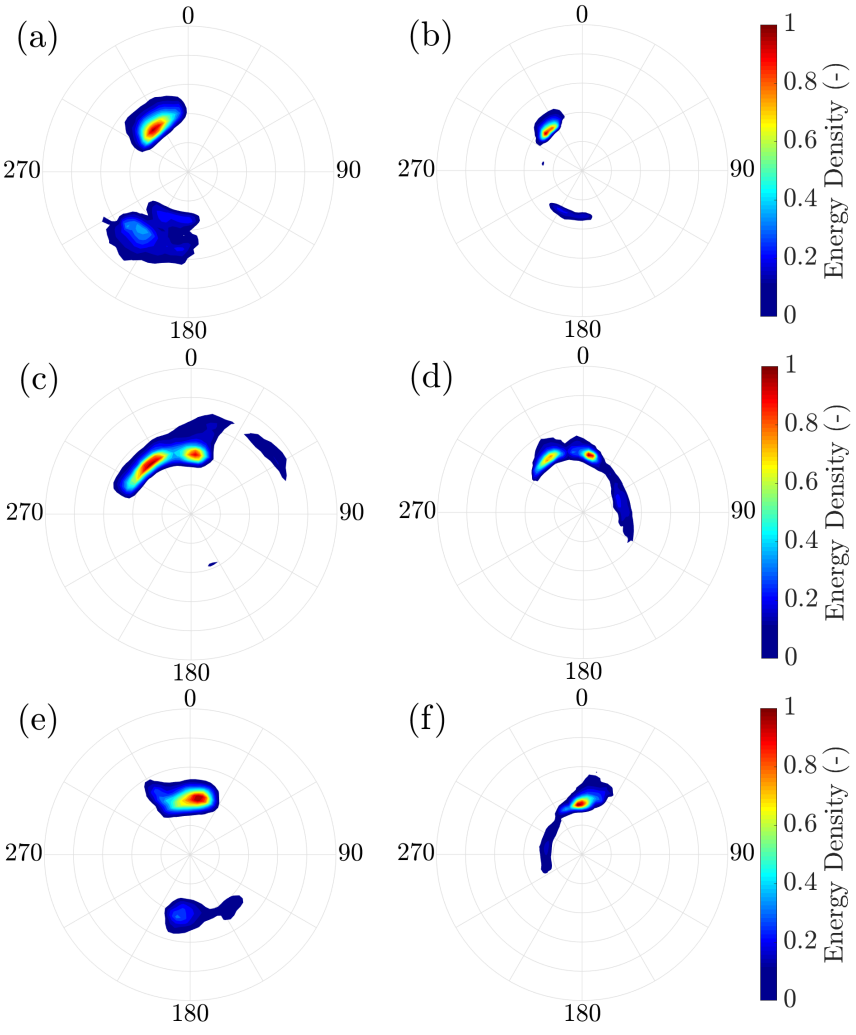


**Figure 8.** Example directional wave energy spectra recorded during ACE (panels a, c, and e) and collocated SAR spectra (panels b, d, and f).

Relatively small bias was detected in leg 1, when sailing along the Antarctic Circumpolar Current. The largest biases (about 0.5 m/s, the same order of magnitude of the current speed itself) were detected primarily at the beginning of leg 1 and at the end of leg 3, where the ship crossed the Agulhas current, and in leg 2, when crossing the Antarctic marginal ice zone.

Current direction is generally in better agreement with satellite observations than speed (see Fig. 11a and b). Differences between WaMoS-II altimeter sensors are normally small throughout the expedition with common values of about 10°. The only substantial differences were recorded at the beginning of leg 3, east of South America.

https://doi.org/10.5194/essd-2020-255
Preprint. Discussion started: 17 October 2020


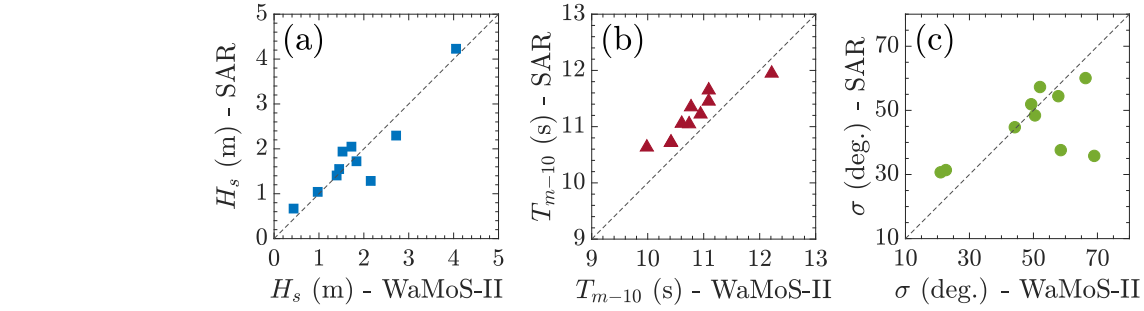


**Figure 9.** Comparison of integrated parameters (WaMoS-II versus SAR): significant wave height ($H_s$, panel a); energy wave period ($T_{m-10}$, panel b); and wave directional spreading ($\sigma_\theta$, panel c)

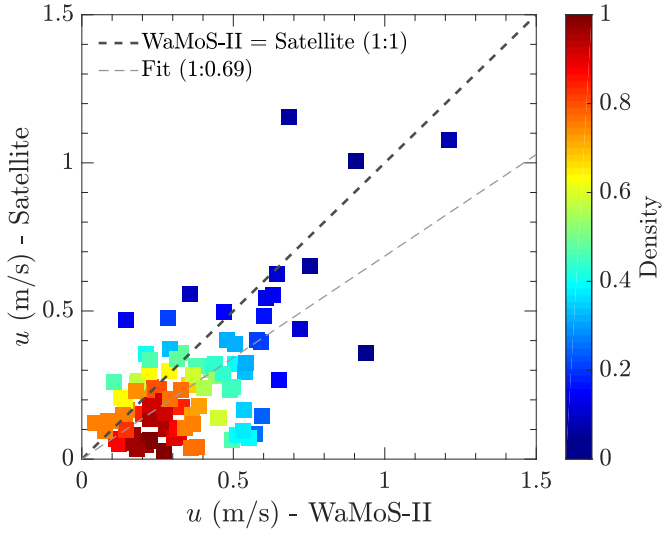


**Figure 10.** Scatter plot of WaMoS-II surface current speeds against observations derived from satellite sensors.

## 6 Conclusions

The scarcity of field observations in the Southern Ocean hampers the accuracy of satellite sensors and prediction models. In response to this issue, a unique data set of sea state parameters, comprising concomitant observations of winds, waves and surface currents, was recorded in the Southern Ocean during the Antarctic Circumnavigation Expedition, from December 2016 to March 2017. Measurements were obtained using a radar-based wave and surface current monitoring system (WaMoS-II) and complemented with records of winds from the meteorological station on board of the research icebreaker Akademik Tryoshnikov. Despite some gaps, observations of wind speeds and directions, directional wave energy spectra, integrated parameters such as wave heights, mean wave periods and wavelengths, and current speeds and directions were collected underway during the entire expedition with outputs every 160 s. The sea state monitoring system was calibrated with benchmark sea state

https://doi.org/10.5194/essd-2020-255
Preprint. Discussion started: 17 October 2020


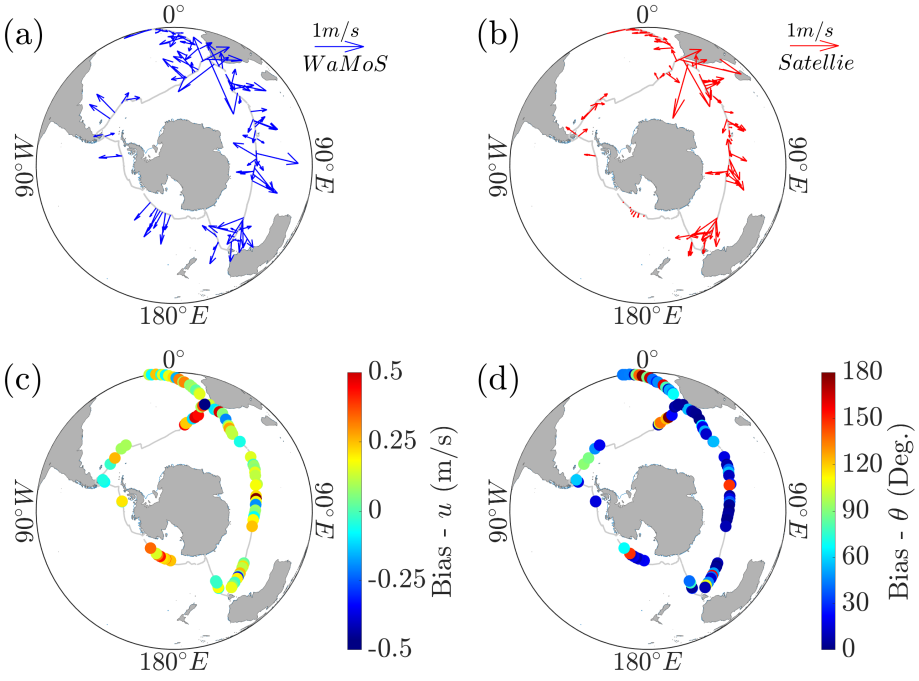


**Figure 11.** Surface current velocities along the ACE voyage: WaMoS-II (a); and space-borne altimeter sensors (b). Surface current biases between WaMoS-II and satellite observations for current speed (c) and direction (d).

records, which were reconstructed from the ship motion. Measurements were also compared against available observations from satellite-borne sensors to verify the roboustness of the database.

The data set includes observations around the Southern Ocean from latitude 34° to 74° South. This includes records in the open ocean across the Antarctic Circumpolar Current and in the Antarctic marginal ice zone. Due to its exposure to strong westerly winds, the Southern Ocean is subjected to harsh sea state conditions all year round. Although the expedition took place during the Austral summer, the data set contains records of severe sea states, in excess of the 90$^{th}$ percentile expected for the season.

The expedition was conceived to bring together a broad range of Earth Science disciplines to explore the interplay of processes in the lower atmosphere, ocean surface, subsurface and land, simultaneously. Additional data sets of processes affected by sea state such as air-sea fluxes, aerosols, ocean chemistry and micro-fibres can be found in Schmale et al. (2019); Rodríguez-Ros et al. (2020); Smart et al. (2020); Thurnherr et al. (2020); and Suaria et al. (2020). The data set presented herein is the most extensive collection of in situ observations of surface processes that is available for the Southern Ocean. On its own or in combination with other concurrent data sets from the Antarctic Circumnavigation Expedition, it can support further theoretical and numerical research on lower atmosphere, air-sea interface and upper ocean processes, contributing to understanding this remote, and yet fundamental for Earth climate, region.

https://doi.org/10.5194/essd-2020-255
Preprint. Discussion started: 17 October 2020


Open Access Earth System Science Data Discussions

## 7 Data availability

Data are available through the Australian Antarctic Data Centre: (i) *Alberello et al. (2020c)* contains data sets of wave spectra including files D1S, D2S, D1M, D2M and FTH (http://dx.doi.org/10.26179/5ed0a30aaf764); and (ii) *Derkani et al. (2020)* contains time series of wind speed and direction, current speed and direction, sea state parameters including wave height, period, wavelength and mean direction for total sea, wind sea and swell systems, ship course, position, and speed for each month of the expedition (http://dx.doi.org/10.26179/5e9d038c396f2).

## Appendix A: WaMoS-II sea state parameters

Details of sea state related variables from WaMoS-II output files as well as integrated parameters are described in Table A1. The $n^{th}$ order moment of the spectral density function, $m_n$, referred to in the table is defined as $m_n = \int\int f^n E(f,\vartheta)\,\mathrm{d}f\mathrm{d}\vartheta$. Directional Fourier coefficients $a$ and $b$ used to compute the wave directional spreading are as follows:

$$a = \int\int \cos(\vartheta)\, S(f,\vartheta)\,\mathrm{d}f\mathrm{d}\vartheta, \tag{A1}$$

$$b = \int\int \sin(\vartheta)\, S(f,\vartheta)\,\mathrm{d}f\mathrm{d}\vartheta. \tag{A2}$$

*Author contributions.* KR, KM and AT participated to the expedition and acquired the data. MHD, AA, LB and AT conceived the manuscript. KGH provided on-shore technical support and LA provided marine forecast during the expedition. MHD and KGH calibarted and analysed the data. FN provided benchmark observation for calibration. LA and SSK provided SAR-spectra. All authors contributed to the data interpretation and to the writing of the manuscript.

*Competing interests.* The authors declare that no competing interests are present.

*Acknowledgements.* This work was supported by the Antarctic Circumnavigation Expedition (ACE) and funded by the ACE Foundation and Ferring Pharmaceuticals. The authors acknowledge contribution from the Australian Antarctic Program (project AAS 4434) and the Cooperative Research Centres Projects, CRC-P, initiative of the Australian Government (project CRC-P53991). MHD was partially supported by a Ph.D. top-up from the Australian Bureau of Meteorology.

https://doi.org/10.5194/essd-2020-255
Preprint. Discussion started: 17 October 2020


Open Access Earth System Science Data Discussions

**Table A1.** WaMoS-II output and integrated sea state related parameters and their symbol, definition, range, and accuracy.

| Sea state related parameter | Symbol | Definition | Range | Accuracy |
|---|---|---|---|---|
| 10 m true wind speed and direction (m/s, °) | $U_{10}, \alpha$ | – | – | – |
| 2-D wave number spectrum ($m^4$) | $E(k_x, k_y)$ | *Refer to Sec. (3.2)* | – | $n/a$ |
| 2-D frequency-direction spectrum ($m^2/(Hz \times rad)$) | $E(f, \vartheta)$ | $\lvert\overrightarrow{k}\rvert \frac{\partial \lvert\overrightarrow{k}\rvert}{\partial \omega} E(k_x, k_y)$ | $0.0078 - 0.5000\,Hz$, $0 - 360°$ | $n/a$ |
| 1-D frequency spectrum ($m^2/Hz$) | $S(f)$ | $\int_0^{360°} E(f, \vartheta)\,\mathrm{d}\vartheta$ | $0.0078 - 0.5000\,Hz$ | $n/a$ |
| Significant wave height (m) | $H_S$ | *Refer to Eq. (2)* | $1 - 20\,m$ | $\pm 0.5\,m$ |
| Energy wave period (s) | $T_{m-10}$ | $T_{m-10} = \frac{m_{-1}}{m_0}$ | $3.5 - 55\,s$ | $\pm 0.5\,s$ |
| Peak wave period (s) | $T_p$ | $\frac{1}{f_p}$ | $3.5 - 55\,s$ | $\pm 0.5\,s$ |
| Mean wave direction (°) | $\beta_m$ | $\arctan(b/a)$ | $0 - 360°$ | $\pm 2°$ |
| Peak wave direction (°) | $\beta_p$ | $\vartheta(f_p)$; $f_p = \frac{1}{T_p}$ | $0 - 360°$ | $\pm 2°$ |
| Peak wave length (m) | $\lambda_p$ | $\lambda_p = \frac{gT_p^2}{2\pi}\sqrt{tanh(\frac{4\pi^2}{T_p^2}\frac{d}{g})}$ | $19 - 600\,m$ | – |
| $1^{st}$, $2^{nd}$ and $3^{rd}$ significant wave height for swell systems 1, 2, and 3 (m) | $H_{s_{1,2,or3}}$ | $4\sqrt{m0_{1,2,or3}}$ | $1 - 20\,m$ | $\pm 0.5\,m$ |
| $1^{st}$, $2^{nd}$ and $3^{rd}$ wave peak period for swell systems 1, 2, and 3 (s) | $T_{p_{1,2,or3}}$ | $\frac{1}{f_{p_{1,2,or3}}}$ | $3.5 - 55\,s$ | $\pm 0.5\,s$ |
| $1^{st}$, $2^{nd}$ and $3^{rd}$ wave length for swell systems 1, 2, and 3 (m) | $\lambda_{1,2,or3}$ | $\frac{2\pi}{\lvert\overrightarrow{k}_{p_{1,2,or3}}\rvert}$ | $19 - 600\,m$ | – |
| $1^{st}$, $2^{nd}$ and $3^{rd}$ wave direction for swell systems 1, 2, and 3 (°) | $\beta_{1,2,or3}$ | $\vartheta(f_{p_{1,2,or3}})$ | $0 - 360°$ | $\pm 2°$ |
| Wave directional spreading $(-)$ | $\sigma_\theta$ | $\sqrt{2[1 - \sqrt{\frac{a^2+b^2}{m_0^2}}]}$ | $0 - 90°$ | $n/a$ |
| Inverse wave age $(-)$ | $\mu$ | $\frac{U_{10}}{c_p}$, $c_p$: *Wave phase velocity* | – | – |
| Wave steepness $(-)$ | $\varepsilon$ | $\overrightarrow{k}\frac{H_S}{2}$ | – | – |
| Surface current speed (m/s) | $u$ | *Refer to Eq. (1)* | $0 - 20\,m/s$ | $\pm 0.2\,m/s$ |
| Surface current direction (°) | $\theta$ | *Refer to Eq. (1)* | $0 - 360°$ | $\pm 2°$ |

## References

Ackley, S. F., Stammerjohn, S., Maksym, T., Smith, M., Cassano, J., Guest, P., Tison, J.-L., Delille, B., Loose, B., Sedwick, P., and et al.: Sea-ice production and air/ice/ocean/biogeochemistry interactions in the Ross Sea during the PIPERS 2017 autumn field campaign, Annals of Glaciology, p. 1–15, https://doi.org/10.1017/aog.2020.31, 2020.

Alberello, A., Onorato, M., Bennetts, L., Vichi, M., Eayrs, C., MacHutchon, K., and Toffoli, A.: Brief communication: Pancake ice floe size distribution during the winter expansion of the Antarctic marginal ice zone., Cryosphere, 13, 2019a.

Alberello, A., Onorato, M., Frascoli, F., and Toffoli, A.: Observation of turbulence and intermittency in wave-induced oscillatory flows, Wave Motion, 84, 81–89, 2019b.

https://doi.org/10.5194/essd-2020-255
Preprint. Discussion started: 17 October 2020




Alberello, A., Bennetts, L., Heil, P., Eayrs, C., Vichi, M., MacHutchon, K., Onorato, M., and Toffoli, A.: Drift of Pancake Ice Floes in the Winter Antarctic Marginal Ice Zone During Polar Cyclones, Journal of Geophysical Research: Oceans, 125, e2019JC015 418, https://doi.org/10.1029/2019JC015418, 2020a.

Alberello, A., Bennetts, L., and Toffoli, A.: Antarctic Circumnavigation Expedition 2017: Motion Sensor and GPS Data, https://doi.org/10.4225/15/5A178EF0E5156, Australian Antarctic Data Centre, 2020b.

Alberello, A., Bennetts, L., Toffoli, A., and Derkani, M.: Antarctic Circumnavigation Expedition 2017: WaMoS Data, Ver. 3, https://doi.org/10.26179/5ed0a30aaf76, Australian Antarctic Data Centre, 2020c.

Babanin, A. V.: On a wave-induced turbulence and a wave-mixed upper ocean layer, Geophys. Res. Lett., 33, 2006.

Babarit, A. and Delhommeau, G.: Theoretical and numerical aspects of the open source BEM solver NEMOH, in: Proc. of the 11th European Wave and Tidal Energy Conference (EWTEC2015), 1968.

Barbariol, F., Benetazzo, A., Bertotti, L., Cavaleri, L., Durrant, T., McComb, P., and Sclavo, M.: Large waves and drifting buoys in the Southern Ocean, Ocean Engineering, 172, 817–828, 2019.

Bennetts, L. G., Alberello, A., Meylan, M. H., Cavaliere, C., Babanin, A. V., and Toffoli, A.: An idealised experimental model of ocean surface wave transmission by an ice floe, Ocean Modelling, 96, 85 – 92, https://doi.org/https://doi.org/10.1016/j.ocemod.2015.03.001, 2015.

Bennetts, L. G., O'Farrell, S., and Uotila, P.: Impacts of ocean-wave-induced breakup of Antarctic sea ice via thermodynamics in a stand-alone version of the CICE sea-ice model, The Cryosphere, 11, 1035–1040, https://doi.org/10.5194/tc-11-1035-2017, 2017.

Collard, F., Ardhuin, F., and Chapron, B.: Monitoring and analysis of ocean swell fields from space: New methods for routine observations, J. Geophys. Res., 114, 2009.

Csanady, G. T.: Air-sea interaction: laws and mechanisms, Cambridge University Press, 2001.

Derkani, M., Alberello, A., and Toffoli, A.: Antarctic Circumnavigation Expedition 2017: WaMoS Data Product, Ver. 1, https://doi.org/10.26179/5e9d038c396f2, Australian Antarctic Data Centre, 2020.

Donelan, M. A., Hamilton, J., and Hui, W. H.: Directional spectra of wind-generated ocean waves, Philos. T. R. SOC. A, 315, 509–562, 1985.

Dong, S., Gille, S. T., and Sprintall, J.: An assessment of the Southern Ocean mixed layer heat budget, J. Clim., 20, 4425–4442, 2007.

Dong, S., Sprintall, J., Gille, S. T., and Talley, L.: Southern Ocean mixed-layer depth from Argo float profiles, J. Geophys. Res., 113, 2008.

Eayrs, C., Holland, D., Francis, D., Wagner, T., Kumar, R., and Li, X.: Understanding the Seasonal Cycle of Antarctic Sea Ice Extent in the Context of Longer-Term Variability, Reviews of Geophysics, 0, https://doi.org/10.1029/2018RG000631, 2019.

Fadaeiazar, E., Leontini, J., Onorato, M., Waseda, T., Alberello, A., and Toffoli, A.: Fourier amplitude distribution and intermittency in mechanically generated surface gravity waves, Phys. Rev. E, 102, 013 106, https://doi.org/10.1103/PhysRevE.102.013106, https://link.aps.org/doi/10.1103/PhysRevE.102.013106, 2020.

Hatten, H., Seemann, J., Horstmann, J., and Ziemer, F.: Azimuthal dependence of the radar cross section and the spectral background noise of a nautical radar at grazing incidence, in: IGARSS'98. Sensing and Managing the Environment. 1998 IEEE International Geoscience and Remote Sensing. Symposium Proceedings.(Cat. No. 98CH36174), vol. 5, pp. 2490–2492, IEEE, 1998.

Hauser, D., Tourain, C., Hermozo, L., Alraddawi, D., Aouf, L., Chapron, B., Dalphinet, A., Delaye, L., Dalila, M., Dormy, E., et al.: New Observations From the SWIM Radar On-Board CFOSAT: Instrument Validation and Ocean Wave Measurement Assessment, IEEE Transactions on Geoscience and Remote Sensing, 2020.

https://doi.org/10.5194/essd-2020-255
Preprint. Discussion started: 17 October 2020




Hessner, K. G., El Naggar, S., von Appen, W.-J., and Strass, V. H.: On the reliability of surface current measurements by X-Band marine radar, Remote Sensing, 11, 1030, 2019.

Holthuijsen, L. H.: Waves in oceanic and coastal waters, Cambridge University Press, Cambridge, 2007.

Humphries, R. S., Klekociuk, A. R., Schofield, R., Keywood, M., Ward, J., and Wilson, S. R.: Unexpectedly high ultrafine aerosol concentrations above East Antarctic sea ice, Atmos. Chem. Phys., 16, 2185–2206, https://doi.org/10.5194/acp-16-2185-2016, 2016.

Khan, S., Hemer, M., Echevarria, E., and King, E.: SAR Surface Waves, https://dx.doi.org/10.26198/5e14142d01539, 2020.

Landwehr, S., Thurnherr, I., Cassar, N., Gysel-Beer, M., and Schmale, J.: Using global reanalysis data to quantify and correct airflow distortion bias in shipborne wind speed measurements, Atmos. Meas. Tech., 13, 3487–3506, 2020.

Li, M., Liu, J., Wang, Z., Wang, H., Zhang, Z., Zhang, L., and Yang, Q.: Assessment of sea surface wind from NWP reanalyses and satellites in the Southern Ocean, J. Atmos. Ocean Tech., 30, 1842–1853, 2013.

Lundy, D.: Godforsaken sea: racing the world's most dangerous waters, Vintage Canada, 2010.

Martinson, D. G. and Wamser, C.: Ice drift and momentum exchange in winter Antarctic pack ice, Journal of Geophysical Research: Oceans, 95, 1741–1755, https://doi.org/10.1029/JC095iC02p01741, 1990.

Massom, R. A. and Stammerjohn, S. E.: Antarctic sea ice change and variability – Physical and ecological implications, Polar Science, 4, 149 – 186, https://doi.org/https://doi.org/10.1016/j.polar.2010.05.001, antarctic Biology in the 21st Century - Advances in and beyond IPY, 2010.

Meiners, K. M., Golden, K. M., Heil, P., Lieser, J. L., Massom, R., Meyer, B., and Williams, G. D.: SIPEX-2: A study of sea-ice physical, biochemical and ecosystem processes off East Antarctica during spring 2012, Deep-Sea Research Part II-Topical Studies in Oceanography, pp. 1–6, https://doi.org/10.1016/j.dsr2.2016.06.010, 2016.

Melville, W. K.: The role of surface-wave breaking in air-sea interaction, Annu. Rev. Fluid Mech., 28, 279–321, 1996.

Meylan, M. H., Bennetts, L. G., and Kohout, A. L.: In situ measurements and analysis of ocean waves in the Antarctic marginal ice zone, Geophys. Res. Lett., 41, 5046–5051, 2014.

Milne, I. A. and Zed, M.: Full-scale validation of the hydrodynamic motions of a ship derived from a numerical hindcast, Ocean Engineering, 168, 83–94, 2018.

Montiel, F., Squire, V. A., and Bennetts, L. G.: Attenuation and directional spreading of ocean wave spectra in the marginal ice zone, Journal of Fluid Mechanics, 790, 492–522, https://doi.org/10.1017/jfm.2016.21, 2016.

Notz, D.: Challenges in simulating sea ice in Earth System Models, Wiley Interdisciplinary Reviews: Climate Change, 3, 509–526, https://doi.org/10.1002/wcc.189, 2012.

Onorato, M., Waseda, T., Toffoli, A., Cavaleri, L., Gramstad, O., Janssen, P. A. E. M., Kinoshita, T., Monbaliu, J., Mori, N., Osborne, A. R., Serio, M., Stansberg, C., Tamura, H., and Trulsen, K.: Statistical properties of directional ocean waves: the role of the modulational instability in the formation of extreme events, Phys. Rev. Lett., 102, https://doi.org/10.1103/PhysRevLett.102.114502, 2009.

Park, Y.-H., Park, T., Kim, T.-W., Lee, S.-H., Hong, C.-S., Lee, J.-H., Rio, M.-H., Pujol, M.-I., Ballarotta, M., Durand, I., and Provost, C.: Observations of the Antarctic Circumpolar Current over the Udintsev Fracture Zone, the narrowest choke point in the Southern Ocean, J. Geophys. Res., 124, 4511–4528, 2019.

Perovich, D. K., Richter-Menge, J. A., Jones, K. F., and Light, B.: Sunlight, water, and ice: Extreme Arctic sea ice melt during the summer of 2007, Geophys. Res. Lett., 35, 2008.

Qiao, F., Yuan, Y., Deng, J., Dai, D., and Song, Z.: Wave–turbulence interaction-induced vertical mixing and its effects in ocean and climate models, Philos. Trans. Royal Soc. A, 374, 20150 201, 2016.

https://doi.org/10.5194/essd-2020-255
Preprint. Discussion started: 17 October 2020




Reichert, K., Hessner, K., Nieto Borge, J. C., and Dittmer, J.: WaMoS-II: A radar based wave and current monitoring system, in: The Ninth International Offshore and Polar Engineering Conference (ISOPE), International Society of Offshore and Polar Engineers, 1999.

Ribal, A. and Young, I. R.: 33 years of globally calibrated wave height and wind speed data based on altimeter observations, Scientific data, 6, 1–15, 2019.

Rio, M.-H., Mulet, S., and Picot, N.: Beyond GOCE for the ocean circulation estimate: Synergetic use of altimetry, gravimetry, and in situ data provides new insight into geostrophic and Ekman currents, Geophysical Research Letters, 41, 8918–8925, 2014.

Rodríguez-Ros, P., Cortés, P., Robinson, C. M., Nunes, S., Hassler, C., Royer, S.-J., Estrada, M., Sala, M. M., and Simó, R.: Distribution and Drivers of Marine Isoprene Concentration across the Southern Ocean, Atmosphere, 11, 556, 2020.

Schmale, J., Baccarini, A., Thurnherr, I., Henning, S., Efraim, A., Regayre, L., Bolas, C., Hartmann, M., Welti, A., Lehtipalo, K., Aemisegger, F., Tatzelt, C., Landwehr, S., Modini, R. L., Tummon, F., Johnson, J. S., Harris, N., Schnaiter, M., Toffoli, A., Derkani, M., Bukowiecki, N., Stratmann, F., Dommen, J., Baltensperger, U., Wernli, H., Rosenfeld, D., Gysel-Beer, M., and Carslaw, K. S.: Overview of the Antarctic Circumnavigation Expedition: Study of Preindustrial-like Aerosols and Their Climate Effects (ACE-SPACE), Bull. Am. Meteorol. Soc., 100, 2260–2283, https://doi.org/10.1175/BAMS-D-18-0187.1, https://doi.org/10.1175/BAMS-D-18-0187.1, 2019.

Schulz, E., Grosenbaugh, M. A., Pender, L., Greenslade, D., and Trull, T. W.: Mooring design using wave-state estimate from the Southern Ocean, Journal of Atmospheric and Oceanic Technology, 28, 1351–1360, 2011.

Schulz, E., Josey, S., and Verein, R.: First air-sea flux mooring measurements in the Southern Ocean, Geophysical research letters, 39, 2012.

Smart, S. M., Fawcett, S. E., Ren, H., Schiebel, R., Tompkins, E. M., Martínez-García, A., Stirnimann, L., Roychoudhury, A., Haug, G. H., and Sigman, D. M.: The Nitrogen Isotopic Composition of Tissue and Shell-Bound Organic Matter of Planktic Foraminifera in Southern Ocean Surface Waters, Geochem. Geophys., 21, e2019GC008 440, 2020.

Suaria, G., Achtypi, A., Perold, V., Lee, J. R., Pierucci, A., Bornman, T. G., Aliani, S., and Ryan, P. G.: Microfibers in oceanic surface waters: A global characterization, Science Advances, 6, https://doi.org/10.1126/sciadv.aay8493, 2020.

Thomas, S., Babanin, A. V., Walsh, K. J. E., Stoney, L., and Heil, P.: Effect of wave-induced mixing on Antarctic sea ice in a high-resolution ocean model, Ocean Dynamics, 69, 737–746, 2019.

Thurnherr, I., Kozachek, A., Graf, P., Weng, Y., Bolshiyanov, D., Landwehr, S., Pfahl, S., Schmale, J., Sodemann, H., Steen-Larsen, H. C., Toffoli, A., Wernli, H., and Aemisegger, F.: Meridional and vertical variations of the water vapour isotopic composition in the marine boundary layer over the Atlantic and Southern Ocean, Atmos. Chem. Phys., 20, 5811–5835, https://doi.org/10.5194/acp-20-5811-2020, https://www.atmos-chem-phys.net/20/5811/2020/, 2020.

Toffoli, A., Babanin, A., Onorato, M., and Waseda, T.: Maximum Steepness of Oceanic Waves: Field and Laboratory Experiments, Geophysical Research Letters, 37, https://doi.org/10.1029/2009GL041771, 2010.

Toffoli, A., McConochie, J., Ghantous, M., Loffredo, L., and Babanin, A. V.: The effect of wave-induced turbulence on the ocean mixed layer during tropical cyclones: Field observations on the Australian North-West Shelf, J. Geophys. Res., 117, 2012.

Toffoli, A., Bennetts, L. G., Meylan, M. H., Cavaliere, C., Alberello, A., Elsnab, J., and Monty, J. P.: Sea ice floes dissipate the energy of steep ocean waves, Geophysical Research Letters, 42, 8547–8554, https://doi.org/10.1002/2015GL065937, 2015.

Toffoli, A., Proment, D., Salman, H., Monbaliu, J., Frascoli, F., Dafilis, M., Stramignoni, E., Forza, R., Manfrin, M., and Onorato, M.: Wind Generated Rogue Waves in an Annular Wave Flume, Phys. Rev. Lett., 118, 144 503, https://doi.org/10.1103/PhysRevLett.118.144503, https://link.aps.org/doi/10.1103/PhysRevLett.118.144503, 2017.

Trowbridge, J., Weller, R., Kelley, D., Dever, E., Plueddemann, A., Barth, J. A., and Kawka, O.: The Ocean Observatories Initiative, Front. Mar. Sci., 6, 74, https://doi.org/10.3389/fmars.2019.00074, https://www.frontiersin.org/article/10.3389/fmars.2019.00074, 2019.

https://doi.org/10.5194/essd-2020-255
Preprint. Discussion started: 17 October 2020




Veron, F.: Ocean spray, Annu. Rev. Fluid Mech., 47, 507–538, 2015.

Vichi, M., Eayrs, C., Alberello, A., Bekker, A., Bennetts, L., Holland, D., de Jong, E., Joubert, W., MacHutchon, K., Messori, G., Mojica, J. F., Onorato, M., Saunders, C., Skatulla, S., and Toffoli, A.: Effects of an explosive polar cyclone crossing the Antarctic marginal ice zone, Geophys. Res. Lett., 46, 5948–5958, 2019.

Wadhams, P.: The Seasonal Ice Zone, pp. 825–991, Springer US, Boston, MA, https://doi.org/10.1007/978-1-4899-5352-0_15, 1986.

Walton, D, W. H. and Thomas, J.: Cruise Report - Antarctic Circumnavigation Expedition (ACE) 20th December 2016 - 19th March 2017, https://doi.org/10.5281/zenodo.1443511, 2018.

Young, I. R. and Ribal, A.: Multiplatform evaluation of global trends in wind speed and wave height, Science, 364, 548–552, 2019.

Young, I. R., Rosenthal, W., and Ziemer, F.: A three-dimensional analysis of marine radar images for the determination of ocean wave directionality and surface currents, Journal of Geophysical Research: Oceans, 90, 1049–1059, 1985.

Young, I. R., Fontaine, E., Liu, Q., and Babanin, A. V.: The Wave Climate of the Southern Ocean, Journal of Physical Oceanography, 50, 1417–1433, 2020.

Yuan, X.: High-wind-speed evaluation in the Southern Ocean, J. Geophys. Res., 109, 2004.

Zieger, S., Babanin, A. V., Rogers, W. E., and Young, I. R.: Observation-based source terms in the third-generation wave model WAVEWATCH, Ocean Modelling, 96, 2–25, 2015.